Hindawi
Mathematical Problems in Engineering
Volume 2019, Article ID 6713231, 18 pages
https://doi.org/10.1155/2019/6713231

*Research Article*

# Braking Efficiency and Stability of Chassis Braking System of Combine Harvester: The Theoretical Derivation and Virtual Prototype Simulation

**Peilong Li and Hongmei Xu**

*College of Engineering, Huazhong Agricultural University/Key Laboratory of Agricultural Equipment in Mid-lower Yangtze River, Ministry of Agriculture and Rural Affairs, Wuhan 430070, China*

Correspondence should be addressed to Hongmei Xu; xhm790912@163.com

Received 23 December 2018; Accepted 6 February 2019; Published 5 March 2019

Academic Editor: Giovanni Berselli



With the advancement of agricultural mechanization, the safety of agricultural vehicles has aroused extensive concern. However, conventional methods evaluate the performance of the combine harvesters in a laborious and inaccurate filed-test way. It is still a challenge to evaluate their performance in a theoretical derivation-based simulation way. Here, we accurately derive the braking model of the combine harvester, which provides a guidance for further braking simulation. Firstly, a four-wheel braking system was designed and theoretically checked. Secondly, the virtual prototype of the chassis braking system was established in ADAMS, in consideration of the complicated contact characteristics between the tire and the road and between the friction pad and the brake disk. Finally, simulation experiments of braking efficiency and directional stability were carried out under different braking conditions. By this means, we find a novel effective yet simple way to optimize the braking efficiency as well as the sufficient braking stability of combine harvesters. The results show that braking efficiency would be improved with stronger braking force, lower initial braking velocity, and lighter weight of the combine harvester. Compared with straight-line braking, steering braking shows lower braking efficiency and less inclination of rear wheel bounce under the same braking conditions. As for braking directional stability, the lateral slippage would be increased with the locking of rear wheels, higher driving speed, or lower road adhesion coefficient. In addition, the simulation results are in agreement with the theoretical results, proving the validity of the virtual prototype simulation. Overall, other than traditional filed-test methods, our method provides an effective yet simple way for designing and evaluating the chassis braking system of combine harvesters.

## 1. Introduction

With the implementation of agricultural mechanization, the use of agricultural machinery such as combine harvesters has become increasingly widespread. To guarantee the safety of combine harvesters, the reliable design of the braking system has received extensive attention. In recent years, several methods have been proposed to evaluate the performance of the combine harvesters in a laborious and inaccurate filed-test way. Moreover, these studies on the braking system of agricultural machinery vehicles are mainly limited to tractors, and most of the studies are focused on the optimization of a certain part of braking system or simulation analysis of the braking efficiency, while there are few studies of the braking system of combine harvesters, particularly the braking directional stability [1–7]. It is still a challenge to evaluate their performance in a theoretical derivation-based simulation way.

We notice that the braking performance of the combine harvesters should be attached much more importance, than that of ordinary vehicles. Different from ordinary vehicles, combine harvesters have higher magnitudes of braking inertia and usually work under low road adhesion coefficient, which may cause longer braking time and braking distance. From the perspective of braking directional stability, the large components such as header, conveyor, and cab of combine

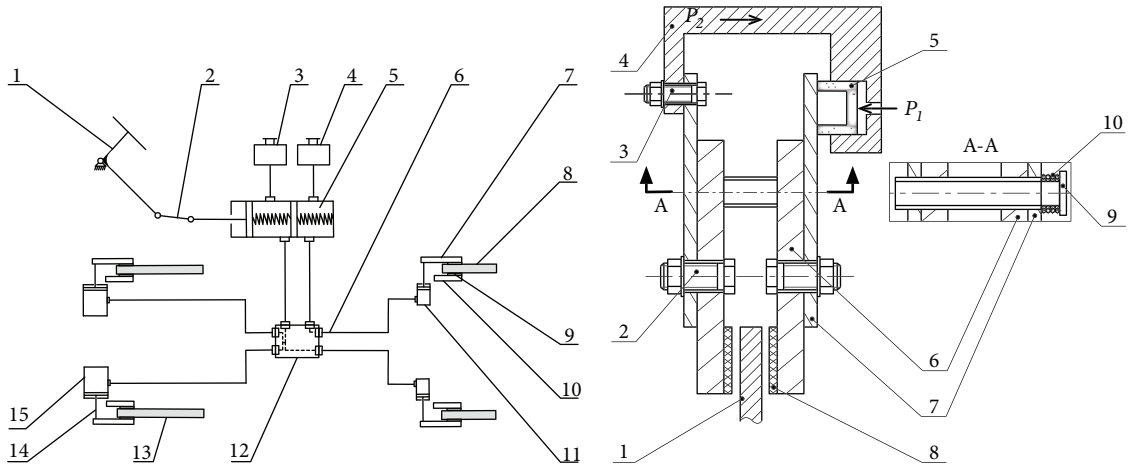


(a) Structural diagram of the chassis braking system of the combine harvester, with 1. brake pedal; 2. brake arm; 3. master oil storage tank; 4. assistant oil storage tank; 5. double-chamber brake master cylinder; 6. braking line; 7. external brake caliper body; 8. rear brake disc; 9. friction pad; 10. internal brake caliper body; 11. rear wheel cylinder; 12. six-way valve; 13. front brake disc; 14. brake push rod (plate); 15. front wheel cylinder.

(b) Structural diagram of the combine harvester's disc brake, with 1. brake disc; 2. fastening bolt I; 3. fastening bolt II; 4. brake caliper body; 5. piston; 6. brake base plate; 7. brake push plate; 8. friction pad; 9. guide rod; and 10. return spring.

Figure 1: Structural diagram of (a) the chassis braking system and (b) the disc brake of the combine harvester.

harvesters are mainly placed in the front part of the combine harvester's body. This feature causes the forward movement of the mass center and reduction of synchronous adhesion coefficient, which may cause the locking of the rear axle [8]. Because the rear axle of a self-propelled combine harvester plays a steering role, if the rear axle is locked first during braking, it will cause not only the sideslip of rear axle, but also the loss of steering capability of the combine harvester, resulting in a dangerous working condition. Currently, most of the China-made tire-type self-propelled combine harvesters are only equipped with brakes on the front axle, which helps to exclude the possibility of the locking of rear axle first but at the expense of braking performance [2, 9].

To improve the braking performance of combine harvesters and at the same time ensure a sufficient degree of braking directional stability, here, a novel effective yet simple method is proposed, to optimize the braking efficiency as well as the sufficient braking stability of combine harvesters. Firstly, the chassis braking system of combine harvesters was designed, for which a virtual prototype model was also established. After that, a series of virtual prototype simulations were carried out to check whether the braking performance of the combine harvesters could meet the national standards and whether the simulation results are in agreement with the theoretical results. Extensive theoretical and simulation results have demonstrated that, other than traditional field-test method, our method can provide an effective way for designing and evaluating the chassis braking system of combine harvesters. Our results are expected to provide references for designing and evaluating the chassis braking system of combine harvesters and shortening the test cycle of braking performance.

## 2. Materials and Methods

*2.1. Structure of Chassis Braking System.* The braking system plays an important part in the braking process of combine harvesters. As the major components used for braking are installed in the chassis, "the braking system" is usually called "the chassis braking system", which explicitly shows the position where the braking system is located. The structure diagram of the chassis braking system is shown in Figure 1(a). The chassis braking system mainly consist of the brake pedal, the brake master cylinder, the brake wheel cylinder, and the brake actuator. Since the force directly applied on the brake pedal is too small to produce enough braking force, the pedal force should be multistage amplified, orderly by the mechanical force amplifier (i.e., the brake arm (2)), and the hydraulic force amplifier (i.e., the brake master cylinder (5) and the brake wheel cylinder (11, 15)), to ensure that the combine harvester is reliably braked. As shown in Figure 1(a), (8) and (13), the brake disks are designed as a caliper-disc-like structure. Taking into consideration the fact that the weight of the combine harvester concentrates in the front (that is to say, the front wheel is subjected to a larger load), a larger braking force should be applied to the front wheel than the rear wheel. In this case, the size (the diameter) of the front brake disc (13) and the front wheel cylinder (15) should be larger than that of the rear brake disc (8) and the rear wheel cylinder (11), to meet the "bigger front force while smaller rear force" design requirement of the combine harvester's chassis braking system [9]. Moreover, it should be noted that the aforementioned design requirement is also the major reason why the chassis braking system of the combine harvester is different from that of the ordinary vehicles, and

Table 1: Design requirements of combine harvester chassis braking system.

| No | Requirement | | Regulation |
|---|---|---|---|
| 1 | The test road surface should be flat and dry, and the adhesion coefficient should not be lower than 0.7 | | GB/T 14248-2008 |
| 2 | At the braking performance test, the combine harvester should be in the following state: the fuel tank is full, and the grain tank is empty. | | |
| 3 | Initial braking velocity | 20 km·h-1 | GB 16151.12-2008 |
| 4 | Braking distance | ≤ 9 m | |
| 5 | Average braking deceleration | ≥ 2.6 m·s-2 | |
| 6 | When the deceleration is lower than 4.5 m·s-2, the rear wheel should not bounce | | |

Table 2: Basic parameters of the combine harvester.

| Parameter | Symbol | Unit | Value | |
|---|---|---|---|---|
| | | | No-load | Full-load |
| Mass | $m$ | kg | 4200 | 5500 |
| Moment of inertia of the chassis to the center of mass | $I_{xx}$ | kg·m2 | 10940 | 15080 |
| Moment of inertia of the chassis to the center of mass | $I_{yy}$ | kg·m2 | 5724 | 7890 |
| Moment of inertia of the chassis to the center of mass | $I_{zz}$ | kg·m2 | 8117 | 10629 |
| Front tread | $h_w$ | mm | 1900 | 1900 |
| Rear tread | $h_w'$ | mm | 1800 | 1800 |
| Wheelbase | $L$ | mm | 2600 | 2600 |
| Height of center of mass | $h_g$ | mm | 680 | 900 |
| Distance from center of mass to front axle | $L_1$ | mm | 900 | 1100 |
| Distance from center of mass to rear axle | $L_2$ | mm | 1700 | 1500 |
| Front load | $G_1$ | kg | 2838 | 3375 |
| Rear load | $G_2$ | kg | 1362 | 2475 |
| Rolling radius of front wheel | $R_{r1}$ | mm | 533 | 533 |
| Rolling radius of rear wheel | $R_{r2}$ | mm | 343 | 343 |

why it is worth to be studied. Specifically, different from the ordinary vehicles, the concentration of the weight in the front of the combine harvester is more likely to cause the locking of the rear axle in braking [8]. As the rear axle of the combine harvester plays a steering role, if in braking, the rear axle locks earlier than the front axle, the combine harvester would not only have a significant sideslip, but also loss the capability of steering (i.e., directional control), which is dangerous and should be avoided in the braking of the combine harvester.

In this study, both the front and rear axle of the analyzed combine harvester were equipped with disc brakes. To make sure that, in braking, the rear axle of the combine harvester locks no earlier than the front axle, the braking force between the front and the rear axle should be reasonably distributed. The structural diagram of the disc brake is shown in Figure 1(b). The brake is mainly composed of a brake block assembly fixed to the chassis or the steering knuckle and a brake disk (1) that rotates with the wheel. The brake block assembly consists of a brake base plate (6), a fastening bolt I (2), and a friction pad (8). The brake disc (1) is fixedly coupled and synchronously rotated with the transmission half shaft, and the brake push plate (7) is fixedly connected to the left and right brake block assemblies by fastening bolt I, and the friction pad (8) is attached to the surface of the brake base plate (6) on the side nearing the surface of brake disc (1). The brake caliper body (4) is fixedly connected to the cylinder block of the wheel cylinder and connected to the right brake block assembly by a translational joint on the same side as the oil input end of the wheel cylinder. The brake block assembly can slide under the constraints of the guide rod (9). When braking, the piston (5) of the brake wheel cylinder is urged by the hydraulic pressure $P_1$ and its reaction force $P_2$ to press the brake disc assembly against the brake disc, and the positive pressure of the compression produces a frictional torque that hinders the movement of the brake disc, which forces the combine harvester to slow down.

*2.2. Design Parameters of the Chassis Braking System.* According to "GB 16151.12-2008 Technical requirements of operating safety for agricultural machinery" and "GBT 14248-2008 Determination of braking performance for harvesting machinery", the design and checking of the chassis braking system are shown in Table 1 [10, 11]. In addition, the braking force distribution curve was used to theoretically check the braking stability of the chassis braking system.

Taking a certain China-made harvester as an example, the basic parameters of the combine harvester are shown in Table 2. With reference to the general design process of chassis braking system, the parameters of the main components of the chassis braking system are shown in Table 3.

Table 3: Parameters of the main components of the chassis braking system.

| Parameter | | Symbol | Unit | Value | |
|---|---|---|---|---|---|
| | | | | Front axle | Rear axle |
| Brake | Diameter of brake disk | $D_b/D_b'$ | mm | 480 | 300 |
| | Thickness of brake disk | $h_b$ | mm | 15 | 15 |
| | Outside diameter of friction pad | $R_{b2}/R_{b2}'$ | mm | 230 | 140 |
| | Inside diameter of friction pad | $R_b1/R_{b1}'$ | mm | 175 | 110 |
| | Effective radius of friction pad | $R_e/R_e'$ | mm | 203.74 | 125.60 |
| | Thickness of friction pad | $b$ | mm | 10 | 10 |
| | Radian of friction pad | $\alpha_b$ | ° | 70 | 70 |
| | Friction factor of friction pad | $f_b$ | -- | 0.6 | 0.6 |
| | Brake factor | $BF$ | -- | 1.2 | 1.2 |
| Brake drive mechanism | Maximum pressure of wheel cylinder | $p$ | MPa | 10 | 10 |
| | Diameter of wheel cylinder | $d_w/d_w'$ | mm | 56 | 25.4 |
| | Diameter of master cylinder | $d_m$ | mm | 30 | 30 |
| | Piston travel of master cylinder | $s_m$ | mm | 30 | 30 |

Table 4: Theoretical calculation results of braking efficiency under different braking conditions.

| Braking force condition | Braking distance (m) | | Braking deceleration (m·s-2) | |
|---|---|---|---|---|
| | II gear | III gear | II gear | III gear |
| Maximum | 1.8981 | 5.3656 | 4.9155 | 4.9155 |
| 60% of maximum | 2.4222 | 7.4648 | 2.9493 | 2.9493 |

*2.3. Theoretical Checking of the Braking Efficiency.* Firstly, from the perspective of braking performance, the design of the chassis braking system was checked. The braking forces $F_{f1}$ and $F_{f2}$ of the front and rear axle were, respectively, calculated according to

$$F_{f1} = 2p\frac{\pi d_w^2}{4}BF\frac{R_e}{R_{r1}} = \frac{1}{2}p\pi d_w^2 BF\frac{R_e}{R_{r1}}$$
$$F_{f2} = 2p\frac{\pi d_w'^2}{4}BF\frac{R'_e}{R_{r2}} = \frac{1}{2}p\pi d_w'^2 BF\frac{R'_e}{R_{r2}} \quad (1)$$

By adjusting the displacement of brake pedal, the pressure $p$ of wheel cylinder in (1) could be changed, and different magnitudes of braking force could be produced. From the perspective of braking distance $S$ and braking deceleration $j$, under the two typical braking force conditions of $p = 10$ MPa (maximum design braking force) and $p = 6$ MPa (60% of maximum design braking force), the theoretical calculation results of braking efficiency of the combine harvester could be obtained by (2) (see Table 4).

$$j = \frac{F_{f1} + F_{f2}}{m}$$
$$S = \left(\tau'_2 + \frac{\tau''_2}{2}\right)v_0 + \frac{v_0^2}{2j} \quad (2)$$

where $(\tau_2' + \tau_2''/2)$ is the brake lag time (0.4 s), $v_0$ is the initial braking velocity ($s^{-1}$), $j$ is the deceleration, and $S$ is the braking distance. For the convenience of description, the initial braking velocity of 20 km·h$^{-1}$ is referred to as "III gear condition", and that of 10 km·h$^{-1}$ is referred to as "II gear condition" in the following analysis with reference to the relevant study [2].

According to the results in Table 4, the braking efficiency of the combine harvester chassis braking system can meet the requirements in Table 1.

*2.4. Theoretical Checking of the Braking Stability.* From the perspective of braking stability, the design of the chassis braking system was checked in this section. The inertial force system of the combine harvester in braking status is shown in Figure 2.

In Figure 2, $u$ is the initial braking velocity; d$u$/d$t$ is the braking deceleration; $F_{B1}$ and $F_{B2}$ are the friction force between the ground and the front wheel and rear wheel during braking, respectively; $F_{N1}$ and $F_{N2}$ are the support force of the horizontal ground to the front and rear wheel during braking, respectively; $G$ ($G = mg$) is the gravity of the combine harvester, where $g$ is the acceleration of gravity (m·s$^{-2}$); $F_j$ is the inertial force of the combine harvester in braking status.

In braking status, the total friction force $F_B$ ($F_B$ equals $F_{B1}$ plus $F_{B2}$, as shown in Figure 2) between the wheels and the ground is the sliding friction force, and its value is no greater than the maximum static friction force $(F_B)_{max}$ between the tire and the ground as shown in (3). Taking the above conditions into account, and taking the torque at the

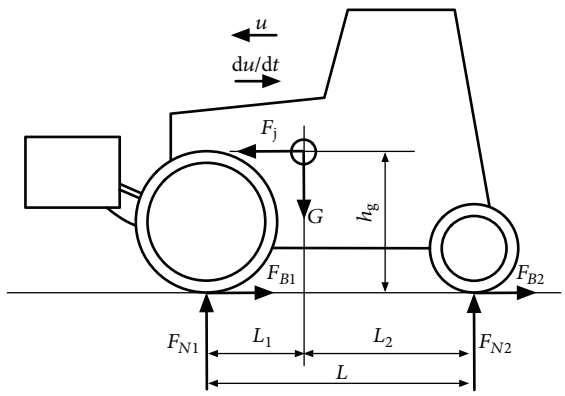


FIGURE 2: Inertial force system of combine harvester in braking status.

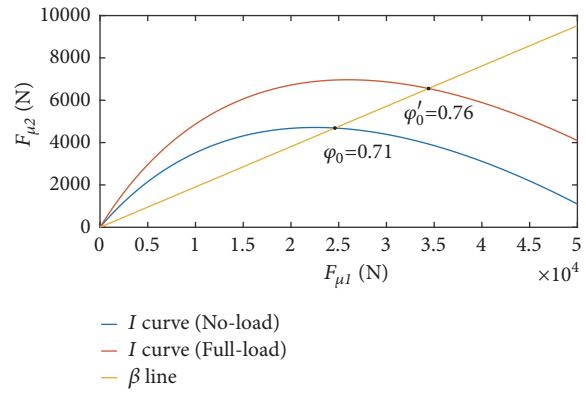


FIGURE 3: Brake force distribution curve.

contact points of the front and rear wheel with the ground, the maximum static friction force on the front and rear axle can be calculated with (4).

$$F_B \le (F_B)_{\max} = F_\phi = \phi(F_{N1} + F_{N2}) \tag{3}$$

$$\begin{aligned} F_{\phi 1} &= \phi F_{N1} = \phi \frac{mg}{L}(L_2 + qh_g) \\ F_{\phi 2} &= \phi F_{N2} = \phi \frac{mg}{L}(L_2 - qh_g) \end{aligned} \tag{4}$$

where $F_{\varphi 1}$ and $F_{\varphi 2}$ are the maximum static friction force between the ground and the front wheel and the rear wheel, respectively; $g$ is the acceleration of gravity; $\varphi$ is the attachment coefficient; and $q$ is the braking intensity, which satisfies the equation $j = qg$.

When the front and rear wheel are locked at the same time, the friction between the ground and wheels and the braking force between the brake disk and friction pad should satisfy the following equation:

$$\begin{aligned} F_{f1} &= F_{B1} = F_{\phi 1} = \phi F_{N1} \\ F_{f2} &= F_{B2} = F_{\phi 2} = \phi F_{N2} \\ F_{N1} + F_{N2} &= mg \end{aligned} \tag{5}$$

where $F_{f1}$ is the braking force between front brake disk and front friction pad and $F_{f2}$ is the braking force between rear brake disk and rear friction pad.

According to (4) and (5), when the front and rear wheel are locked at the same time, the relationship between $F_{f1}$ and $F_{f2}$ is shown in

$$F_{f2} = \frac{1}{2}\left[\frac{mg}{h_g}\sqrt{L_2^2 + \frac{4h_g L}{mg}F_{f1}} - \left(\frac{mgL_2}{h_g} + 2F_{f1}\right)\right] \tag{6}$$

where $F_{f1}$ and $F_{f2}$ are presented with the unit of kN.

According to (6), with $F_{f1}$ as the abscissa and $F_{f2}$ as the ordinate, the braking force distribution curve ($I$ curve) can be drawn (Figure 3), which reflects the relationship between the front and rear wheels in braking force when they are both locked.

For the chassis braking system discussed in this study, the ratio of braking force of the front and rear wheel brakes is constant, which is often called the braking force distribution coefficient $\beta$. The braking force of the front ($F_{f1}$) and rear wheel ($F_{f2}$) can be calculated with (1), and $\beta$ can be calculated by (7). According to (7), the relationship between $F_{f1}$ and $F_{f2}$ is shown as a straight line passing through the origin in Figure 3, which is called $\beta$ line. In Figure 3, the road adhesion coefficient indicated by the intersection point ($F^{\beta}{}_{f1}$, $F^{\beta}{}_{f2}$) of the $\beta$ line and the $I$ curve is just the synchronous adhesion coefficient of the chassis braking system.

$$\beta = \frac{F_{f1}}{F_{f1} + F_{f2}} \tag{7}$$

Figure 3 shows that the synchronous adhesion coefficient of the designed combine harvester is 0.71 and 0.76 under no-load and full-load conditions, respectively, which are both greater than the minimum required value of 0.7 in Table 1. According to Table 1, when the road adhesion coefficient is no lower than 0.7, it can be ensured that the locking of the front wheel will occur before that of the rear wheel.

In addition, when rear wheel bounce occurs during braking, there should be $F_{N2} = 0$. When substituting $F_{N2} = 0$ into (4) and taking the equation $j = qg$ into account, the deceleration at rear wheel bounce can be presented by

$$j = \frac{L_2 g}{h_g} \tag{8}$$

According to (8) and Table 2, when the rear wheels of the combine harvester bounce, the theoretical braking deceleration should not be lower than 24.5 m·s$^{-2}$ and 16.3 m·s$^{-2}$ under no-load and full-load conditions, respectively. In this case, under all the braking conditions in Table 4, the calculation results show that rear wheel bounce will not occur in theory, which meets the requirements in Table 1.

### 2.5. Establishment of Virtual Prototype of the Chassis Braking System

*2.5.1. Establishment of Geometrical Models.* The geometrical model of the combine harvester chassis braking system is

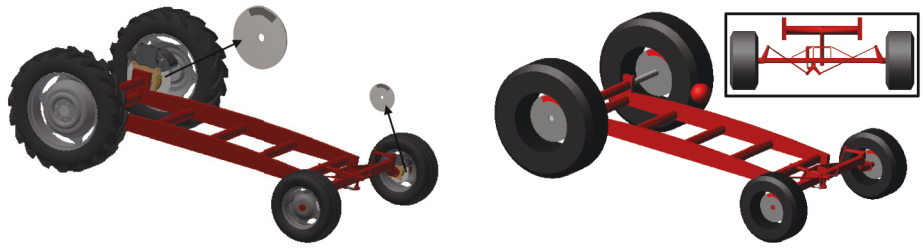

(a) (b)

Figure 4: Simplification of chassis braking system: (a) before simplification and (b) after simplification.

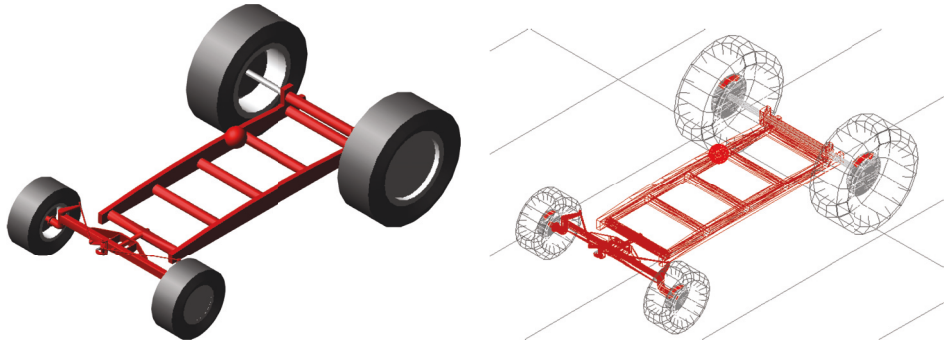

(a) (b)

Figure 5: Virtual prototype model of the chassis braking system of combine harvester: (a) shaded pattern; and (b) wire-frame pattern.

mainly composed of the chassis frame and the rear steering axle as shown in Figure 4(b). Compared with Figure 4(a), Figure 4(b) mainly includes simplifications from two aspects. Firstly, the chassis and the body are simplified as a mass substitute ball. Secondly, the production of braking force is simplified to the contact between brake disk and friction pad.

*2.5.2. Import of Geometrical Model.* In this study, the geometrical model of the combine harvester chassis braking system was saved as an intermediate file in Parasolid format and then imported into ADAMS/View for virtual prototype establishment.

The realization of braking depends on a complex contact process between the tire and the road surface. When the combine harvester is in operation, the relaxing effect of tires has a significant influence on the slip rate due to the low working velocity. Because the slip rate can affect the adhesion coefficient, which further influences the braking performance, the relaxing effect of the tires should be well defined in the virtual prototype model [12]. In this case, the UA tire in the ADAMS tire library was used instead of the tire geometrical model established in PRO/E. The mechanical parameters of the UA tire which are calculated by empirical formulas are shown in Table 5, according to the relevant studies and existing harvester designs [13–18].

In addition, according to Table 1, the 2d_flat road surface in the ADAMS road library was selected as the testing road during the virtual prototype simulation. The adhesion coefficient of the testing road was adjusted by changing the "MU" value in the data subblock "[PARAMETER]" of the road file "2d_flat.rdf". The virtual prototype model is shown in Figure 5.

In Table 5, CSLIP is the longitudinal slip stiffness; CALPHA is the cornering stiffness; and CGAMMA is the camber stiffness.

*2.5.3. Attribute Definition and Constraint Addition.* For the geometrical model imported into ADAMS from Parasolid format files, the mass information of the components is set as 'User Input' by defaults and thus needs to be redefined by the user. To achieve correct contact between the combine harvester and the road surface, the mass attributes of each component and the acceleration of gravity must be set correctly. In addition, each component should be represented by a color so that it can be distinguished from other components.

According to the motion relationship between different components in the chassis braking system, constraints were added to the virtual prototype model (see Table 6).

*2.5.4. Addition of Force and Motion.* To facilitate the adjustment of the mass, steering angle, braking force, braking start time and other experimental variables of the virtual prototype, and to simulate the uneven distribution of braking force, rear wheel locking and other conditions, the variables are defined in ADAMS (see Table 7).

In Table 7, *mass_modify_ratio* realizes the conversion of no-load and full-load status of the combine harvester; $brake_s$ ensures that the combine harvester reaches the required

Table 5: Mechanical parameters of UA tire.

| Parameter | Symbol | Unit | Value | |
|---|---|---|---|---|
| | | | Front wheel | Rear wheel |
| Vertical stiffness | $k_r/k_r'$ | kN/m | 402.32 | 275.45 |
| CSLIP | $k_l/k_l'$ | kN/m | 626.66 | 576.49 |
| CALPHA | $k_a$ | N/rad | $1.2\times10^5$ | $6\times10^4$ |
| CGAMMA | $k_g$ | N/rad | $1.2\times10^4$ | $6\times10^3$ |
| Vertical damping | $\zeta$ | -- | 0.04 | 0.04 |
| Rolling resistance | $f_r$ | -- | 0.16 | 0.16 |
| Static friction coefficient | $\mu_0$ | -- | 0.95 | 0.95 |
| Dynamic friction coefficient | $\mu_1$ | -- | 0.75 | 0.75 |

Table 6: Constraints added to the virtual prototype of chassis braking system.

| Constraint objects | | Constraint type | Constraint quantity |
|---|---|---|---|
| Object 1 | Object 2 | | |
| Chassis body | Front axle | Fixed joint | 1 |
| | Mass substitute ball | Fixed joint | 1 |
| | Steering axle body | Revolution joint | 1 |
| | Cylinder body | Revolution joint | 1 |
| Steering axle body | Steering pivot | Revolution joint | 1 |
| | Left/Right steering knuckle | Revolution joint | 2 |
| Cylinder rod | Cylinder body | Translational joint | 1 |
| Cylinder rod | Steering pivot | Inline | 1 |
| Steering pivot | Left/Right tie rod pair | Spherical joint | 2 |
| Left/Right tie rod pair | Left/Right pull arm | Spherical joint | 2 |
| Left/Right pull arm | Left/Right steering knuckle | Fixed joint | 2 |
| Front wheel | Front axle | Revolution joint | 2 |
| Rear wheel | Left/Right steering knuckle | Revolution joint | 2 |
| Left tie rod | Right tie rod | Revolution joint | 2 |
| Front friction pad | Front axle | Translational joint | 4 |
| Rear friction pad | Left/Right steering knuckle | Translational joint | 4 |
| Brake disk | Tire | Fixed joint | 4 |
| Road | Ground | Fixed joint | 1 |
| | Total | | 34 |

velocity before braking; $s$ is used to adjust the braking force; *steer_lock* is a 0 or 1 variable, and when it equals 1, the steering wheel is locked; when it equals 0, the steering wheel is unlocked; *steer_angle* determines the rotation angle of the steering pivot.

In order to obtain a required velocity before braking, a pair of identical driving torques was defined at the two joints of the front wheel and axle. "Body Fix" was selected as the torque action mode, and the torque value was defined by the following function in ADAMS:

$$IF\left(time - brake_s: 8000, 0, 0\right) \tag{9}$$

IMPACT collision function was chosen to describe the contact process [19–23]. At this time, the friction coefficient between the friction pad and the brake disc has a nonlinear relationship with their sliding speed, which is similar to the real situation. A total of 8 contacts were applied to the virtual prototype. The contact parameters of the front wheel brake were defined as in Table 8.

In the IMPACT collision function, the contact force is related to the penetration of the two objects. In the braking simulation, only the levels of braking force are concerned, while the generation way of braking force is not concerned. Therefore, the contact force can be controlled by adjusting the penetration between the two objects. To correctly describe the generation process of the braking force between the friction pad and brake disc, the displacement driving function of the front and rear friction pad was defined as follows in ADAMS:

$$disp\left(time\right) = STEP\left(time, brake_s, 0, brake_s + 0.4, s\right) \tag{10}$$

Because of the positive correlation between the braking force and contact stiffness, to achieve a reasonable distribution of braking force, only the contact stiffness was set different in setting the contact parameters of the front and rear axle. The

Table 7: Variable definition for the virtual prototype of combine harvester braking system.

| Parameter | Symbol | Unit |
|---|---|---|
| Mass adjustment factor | *mass_modify_ratio* | -- |
| Braking start time | $brake_s$ | s |
| Braking force | *s* | -- |
| Braking force distribution coefficient | *brake_distribution* | -- |
| Steer wheel locking flag | *steer_lock* | -- |
| Steering angle | *steer_angle* | ° |

Table 8: Definition of contact parameters between friction pad and brake disc.

| Parameter | Symbol | Unit | Value |
|---|---|---|---|
| Contact stiffness | *Stiffness* | $N \cdot m^{-1}$ | $7 \times 10^8$ |
| Exponent | *Exponent* | -- | 2 |
| Damping | *Damping* | $N \cdot s \cdot m^{-1}$ | $2.8 \times 10^4$ |
| Permeation amount when damping is fully effective | *Penetration* | m | $1.5 \times 10^{-4}$ |

relationship of the stiffness parameters between the front and rear axle is shown in (11) in ADAMS.

$$Stiffness' = \frac{1 - brake\_distribution}{brake\_distribution} Stiffness \quad (11)$$

In addition, the driving function of the rear wheel steering was defined as follows in ADAMS:

$$disp\,(time) = STEP\,(time, 0, 0, 10, -steer\_angle) \quad (12)$$

## 3. Results and Discussion

*3.1. Simulation Results and Discussion of the Braking Efficiency.* In the virtual prototype simulation of braking efficiency, the road adhesion coefficient was set at 0.7, which meets the requirements described in Table 1. In order to verify the effectiveness of the setting of road adhesion coefficient, the influence of different road adhesion coefficients (0.7~1) on braking distance was investigated under the same braking conditions (20 $km \cdot h^{-1}$ braking initial velocity, full-load, 60% of maximum braking force) (Figure 6). As shown in Figure 6, the braking distance increases with decreasing road adhesion coefficient. Therefore, the road adhesion coefficient in the virtual prototype was set at 0.7 to ensure the reliability of the check of braking efficiency.

Figures 7 and 8, respectively, show the straight-line braking efficiency and steering braking efficiency of full-load combine harvester under different working conditions and braking forces.

In Figures 7 and 8, the inflection point of velocity curve corresponds to the effective time of braking. After this moment, the slope of the displacement curve decreases gradually; the velocity of the combine harvester declines, and the deceleration curve rises with fluctuations. It should be noted that compared with the displacement curve and velocity curve, the deceleration curve shows more obvious fluctuations. When the brakes are not in effect, the deceleration curve fluctuates around 0 under the stimulation of the road and tire. When braking, the deceleration curve fluctuates in a certain range above 0, and at the same time, the velocity curve declines continuously. In addition, when the braking force decreases, deceleration will be reduced proportionally, and it takes more time for the combine harvester to slow down. When braking is over, the deceleration curve fluctuates around 0 again. The following pages (the second part of Model Validation) will prove that these fluctuations are due to contact characteristics such as stiffness, damping, and tire relaxation. The selected UA tire in the virtual prototype can well present the above characteristics.

Based on Figures 7 and 8, the key parameters of the braking efficiency are intuitively shown in Table 9. Note that, in Table 9, the braking deceleration is presented as the peak value of the deceleration curve in Figures 7 and 8. This is because the peak deceleration is easily acquired in the fluctuant curves, and it can effectively reveal the relative magnitude of the deceleration among different braking conditions. Moreover, the peak deceleration is regarded as a more comprehensive reflection of the braking stability, which is further discussed in the following sections (Rear wheel bounce).

Figure 7 and Table 9 show that at a certain gear speed, the greater the braking force is, the shorter the braking time and braking distance will be, and the lower the peak braking acceleration will be; at a certain braking force, higher braking initial velocity will result in longer braking time and braking distance, and higher peak braking acceleration. In addition, under the various braking conditions listed in Table 9, the braking efficiency of the combine harvester meets the requirements in Table 1.

As shown in Table 9, compared with straight-line braking, steering braking takes more time and longer distance to stop the combine harvester under the same braking conditions. Therefore, compared with straight-line braking, steering braking has a lower braking efficiency because lateral friction is smaller than longitudinal friction between the road and tire [15, 24, 25] .

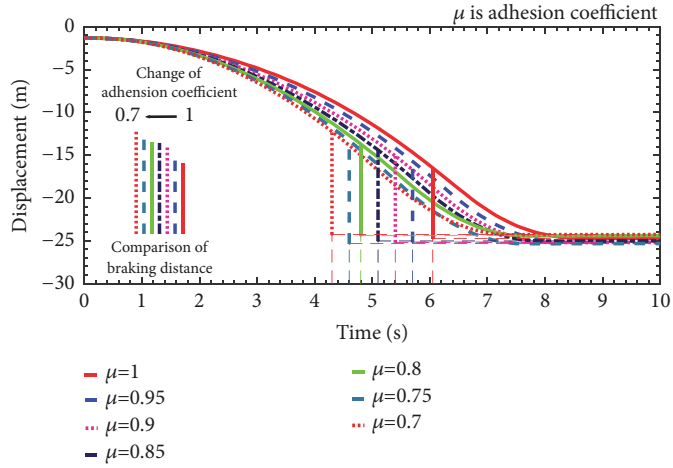


Figure 6: Influence of road adhesion coefficients on braking distance.

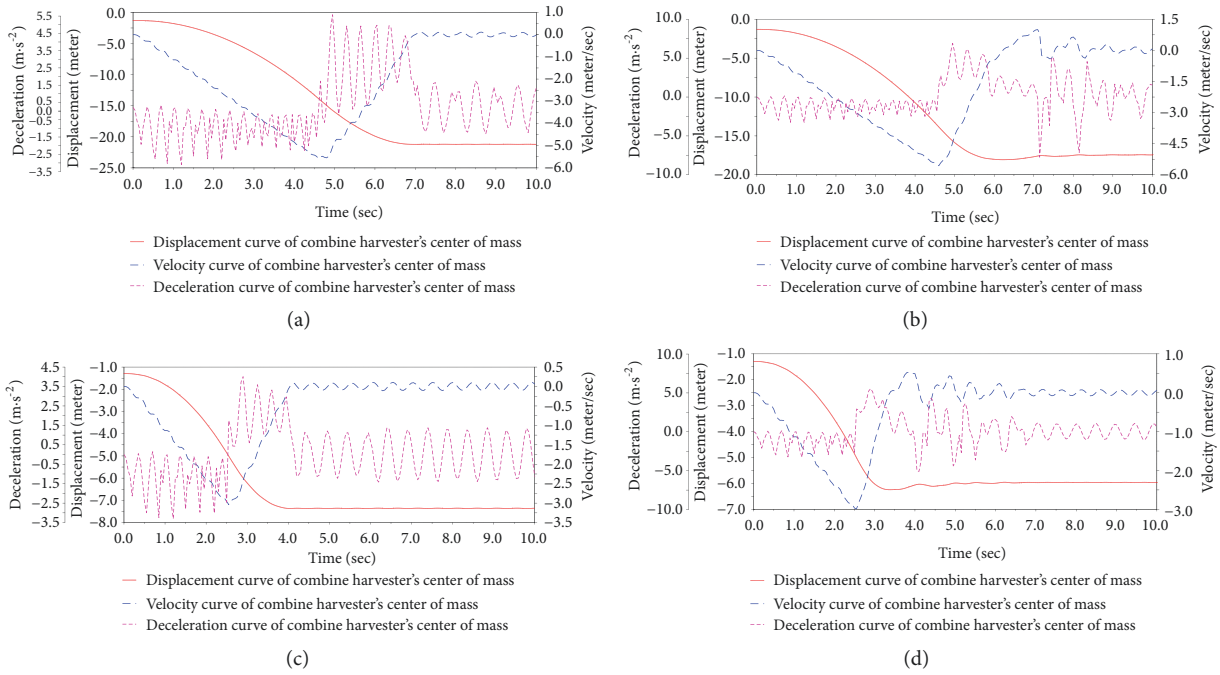


Figure 7: Full-load straight-line braking efficiency curve under different braking conditions: (a) 60% of maximum design braking force, III gear condition; (b) maximum design braking force, III gear condition; (c) 60% of maximum design braking force, II gear condition; and (d) maximum design braking force, II gear condition.

*3.2. Model Validation.* To validate the effectiveness of the simulated virtual prototype model, the simulated results (in Table 9) are compared with the theoretical results (in Table 4). To make the comparison clear, the simulated and the theoretical results are represented in Table 10. Moreover, to specifically quantify the agreement between the two results in an objective way, the percentage differences of the theoretical results against the simulated results are calculated in Table 10.

It should be pointed out that, in Table 10, the results of braking deceleration as shown in Tables 9 and 4 are not used for comparison. This is because in Table 9, the braking deceleration is presented as the peak value of the deceleration curve in Figures 7 and 8. Since the deceleration curves are fluctuant at the combine harvester's center of gravity, we found that, it is the median value (not the peak value) of the deceleration curve that is comparable with the theoretical results. In the following pages (the second part of Model Validation), we will discuss why the median value makes sense, and how the median value removes the disturbance of tire stiffness and damping (factors causing deceleration curves fluctuations). As the theoretical results are calculated leave out of the consideration of tire stiffness

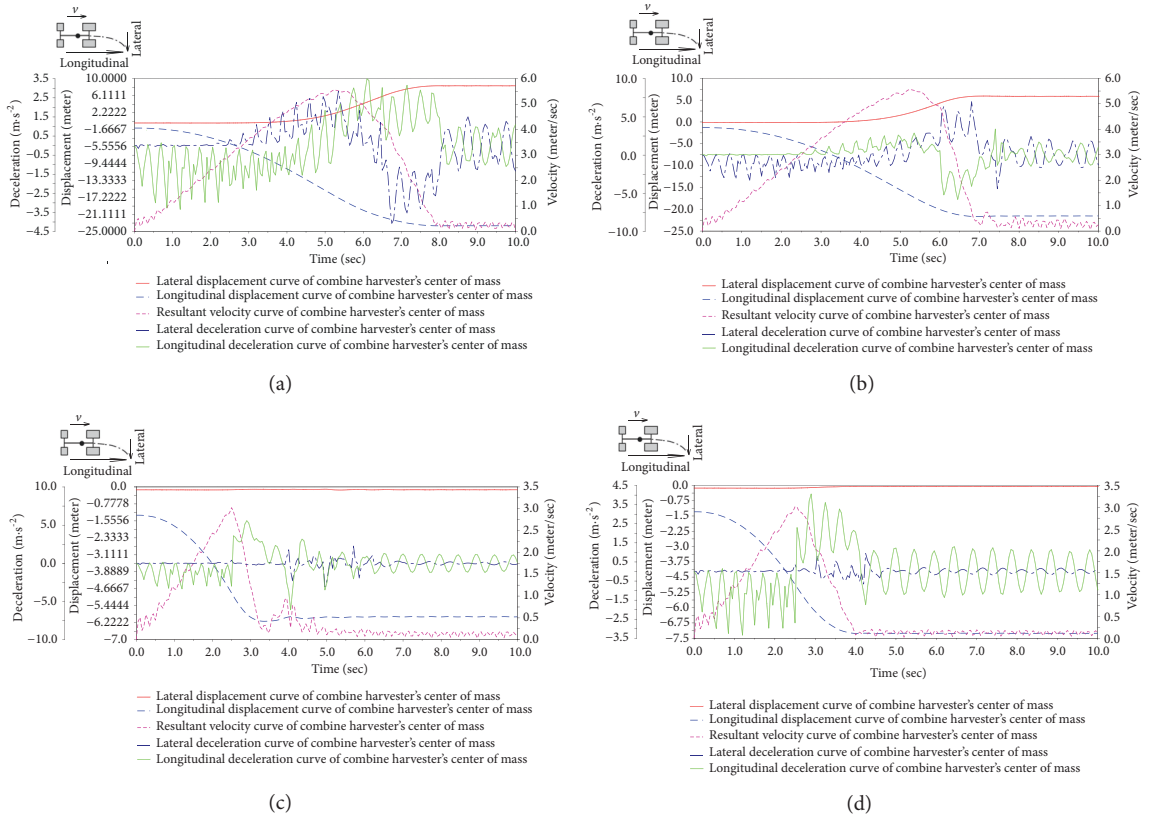


Figure 8: Full-load steering braking efficiency curve under different braking conditions: (a) 60% of maximum design braking force, III gear condition; (b) maximum design braking force, III gear condition; (c) 60% of maximum design braking force, II gear condition; and (d) maximum design braking force, II gear condition.

Table 9: Comparison of efficiencies between simulated steering braking and straight-line braking.

| Braking force condition | | Braking time (s) | | Braking distance (m) | | Peak braking deceleration (m·s$^{-2}$) | |
|---|---|---|---|---|---|---|---|
| | | II gear | III gear | II gear | III gear | II gear | III gear |
| Straight-Line | Maximum | **0.95** | **1.80** | **1.6731** | **5.3009** | **5.5234** | **6.9006** |
| | 60% of maximum | 1.60 | 2.55 | 2.7941 | 8.4496 | 4.0105 | 5.3644 |
| Steering | Maximum | **1.15** | **1.65** | **1.8629** | **6.1738** | **6.0128** | **7.7125** |
| | 60% of maximum | 1.70 | 2.75 | 2.9734 | 9.3305 | 4.1546 | 4.5025 |

and damping, for the braking deceleration, the percentage differences between the median value and the theoretical results are comfortable, as shown in Table 11.

*3.2.1. Validation of the Braking Distance.* It can be shown in Table 10 that, at the III gear speed, the theoretical and simulated straight-line braking distance of the combine harvester is 5.3656 m and 5.3009 m (1.22% difference) with the maximum design braking force, while being 7.4648 m and 8.4496 m (11.65% difference) with 60% of maximum design braking force, respectively. And at the II gear speed, the theoretical and simulated straight-line braking distance of the combine harvester is 1.8981 m and 1.6731 m (13.45% difference) with the maximum design braking force, while being 2.4222 m and 2.7941 m (13.31% difference) with 60% of maximum design braking force, respectively. Thus, it can be concluded that the difference between the simulated results and the theoretical results of straight-line braking is between 1.22% and 13.45%, under various braking conditions.

*3.2.2. Validation of the Braking Deceleration.* Different from the braking distance, as aforementioned, in the simulation results, the braking deceleration curve shows fluctuations (as shown in Figure 7). Hence, in the braking stage, there is no certain deceleration value to be compared with the related theoretical value. In Table 9, the peak deceleration is utilized for representing the relative magnitude of the deceleration among different braking conditions, and the occurrence of the rear wheel bounce. However, the peak braking deceleration extracted from the simulated results is

Table 10: Comparison of braking distance between simulated results and theoretical results.

| Magnitude of the braking force | Calculation method | Braking distance (m) | |
|---|---|---|---|
| | | II gear | III gear |
| Maximum design | Theoretical | 1.8981 | 5.3656 |
| | Simulated (Peak) | 1.6731 | 5.3009 |
| | *Percentage difference* | **13.45%** | **1.22%** |
| 60% of maximum design | Theoretical | 2.4222 | 7.4648 |
| | Simulated (Peak) | 2.7941 | 8.4496 |
| | *Percentage difference* | **13.31%** | **11.65%** |

Table 11: Comparison of braking deceleration between simulated results and theoretical results.

| Magnitude of the braking force | Calculation method | Braking deceleration ($m \cdot s^{-2}$) | |
|---|---|---|---|
| | | II gear | III gear |
| Maximum design | Theoretical | 4.9155 | 4.9155 |
| | Simulated (Peak) | 4.2986 | 4.5849 |
| | *Percentage difference* | **14.35%** | **7.21%** |
| 60% of maximum design | Theoretical | 2.9493 | 2.9493 |
| | Simulated (Peak) | 2.5083 | 2.8732 |
| | *Percentage difference* | **17.58%** | **2.65%** |

not suitable for comparing with the theoretical results. This is because the theoretical calculation does not comprehensively consider the contact characteristics between the tire and the road. Specifically, the peak braking deceleration in the simulated results, consist of not only the constant component arising from the capsizing moment (which the theoretical results also consider), but also the fluctuant component arising from the contact characteristics (which the theoretical results does not consider).

So far, one might wonder: Question 1. How can we prove that the deceleration curves fluctuations in the simulation are relevant to the contact characteristics, such as the stiffness and the damping between the tire and the road? Question 2. How can we extract the constant component from the fluctuant deceleration curves, leave out of the disturbance of the stiffness and the damping, so that the extracted value from the simulated results can be comparable with the theoretical results?

Fortunately, by comparing the variation regularity of the deceleration curves, to that of the supporting force curve acting on the harvester's tire, we find the answer of the two questions.

To answer Question 1, Figure 9 proves that the deceleration curves fluctuations are relevant to the contact characteristics. As the supporting force acting on the rear wheel makes the extremum value at the same time with that on the front wheel, in Figure 9, only the supporting force of the front wheel is sufficient for representing the variation of the supporting force.

In Figure 9, the deceleration curves synchronously fluctuate with the supporting force. In other words, the local extremum values (peaks or valleys) of the deceleration curve and its related supporting force curve occur at the same time. As the contact model between the tire and the road can be regard as a parallel combination of the spring (stiffness) and the damper (damping), as shown in the top right of Figure 9, the supporting force acting on the wheel is a direct reaction from the contact characteristics (stiffness and damping). In this case, Figure 9 can also explicitly prove that the fluctuations of the deceleration curves are closely related to and caused by the contact characteristics.

Specifically, as shown in Figure 9(a) or 9(b), before the braking stage (when no brake force is applied), the peak (valley) value of the supporting force is corresponding to the valley (peak) value of the deceleration; in the braking stage, the peak (valley) value of the supporting force is corresponding to the peak (valley) value of the deceleration. These two situations are not contradicted. This is because, before the braking, the deceleration is negative, so that the negative valley actually represents a greater deceleration; while in the braking, the deceleration is positive, so that the positive peak represents a greater deceleration. In short, the peak of the supporting force results in a local peak of deceleration, and vice versa. And as the supporting force fluctuates with the oscillating movement of the spring-damper model (the contact model between the tire and the road), the deceleration also fluctuates simultaneously.

Now we will explain the causes of the corresponding relationship between the supporting force and the deceleration. The greater the supporting force (i.e., the superposition of the stiffness and the damping) is, the larger the deformation of the spring and the damper in the tire model. As both the spring and the damper are energy-storage elements, larger deformation means more energy stored. According to the law of conservation of energy, the larger energy is converted and stored in the spring-damper, the smaller the kinetic energy

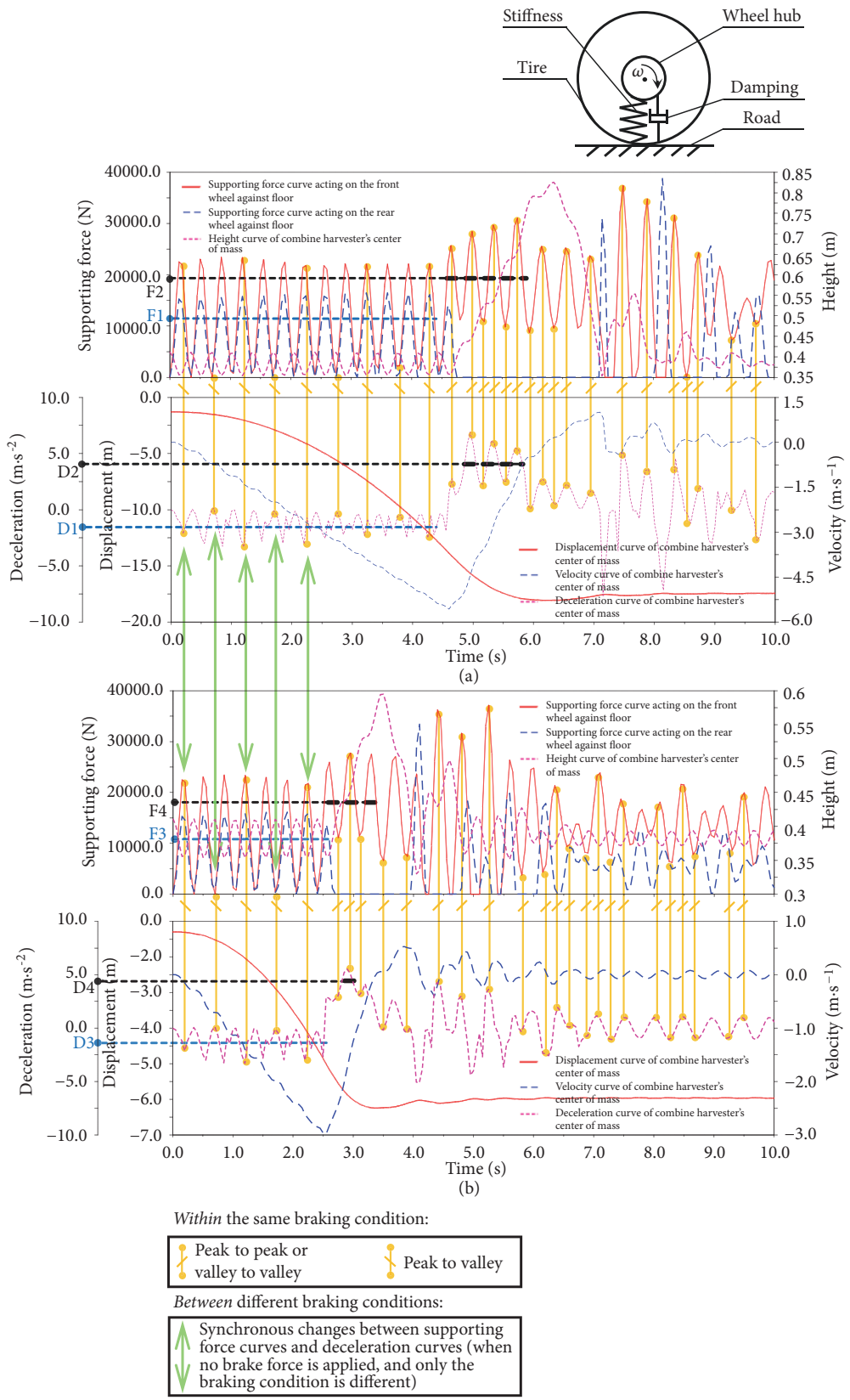


Figure 9: Analysis of the causes of the deceleration curves fluctuations. (a) Maximum design braking force, III gear condition, straight-line braking; (b) maximum design braking force, II gear condition, straight-line braking. D1, D3 and F1, F3 represent the middle value of the fluctuant deceleration and supporting force, respectively, under the stage before braking. D2, D4 and F2, F4 represent the same as above, under the stage in braking.

(which is related to the velocity) of the combine harvester is. Hence, the peak of the supporting force is related to a large instantaneous rate of the velocity change (i.e., a large deceleration).

Moreover, as shown in the green arrows in Figure 9, we also find that, in the stage before braking, the deceleration curves shapes between different braking conditions (between the Figures 9(a) and 9(b)) are similar, so are the supporting force curves. Note that the only difference of the braking conditions between the Figures 9(a) and 9(b) lies in the initial braking velocity (II or III gear condition). This similarity does make sense, because the fluctuations of the two curves mainly depend on the inherent characteristic of the stiffness and the damping, while being independent of the initial braking velocity. Within the same braking conditions, in the stage of braking, the middle value of the fluctuant deceleration curve is obvious higher than that in the stage before braking (when the brakes are not in effect). This is caused by the additional braking force.

To answer Question 2, an insight into the contact model between the tire and the road is required. The supporting force results from four factors, the gravity, the capsizing moment, the stiffness, and the damping. Since the former two factors (gravity and capsizing moment) does not have the characteristics of reciprocating cyclic fluctuations, they belong to the constant direct component, which represents as the middle value of the fluctuant deceleration curve. The so-called "middle value" is a central position around which the deceleration curve fluctuates at a certain stage (the stage before or in braking). In other words, the "middle value" is related to the equilibrium position of the spring-damper contact model, so that it is independent of the contact characteristics. Since it is the spring-damper nature to be oscillating, the latter two factors (stiffness and damping) belong to the alternating component, which results from the contact characteristics and results in the deceleration curves fluctuations.

Hence, the middle value of the deceleration curve is deemed as having the same physical meanings with the theoretical calculation, which excludes the influence of the contact characteristics. That is to say, as for the deceleration, the middle value extracted from the simulation result, is comparable with the theoretical results. As shown in Figure 9, in the stage before braking, the middle values of the wavelike deceleration curves are D1 and D3 respectively, which are both around -1.2 $m{\cdot}s^{-2}$. This middle value (-1.2 $m{\cdot}s^{-2}$) is reasonable, because it approximately equals the slope of the velocity curve, after fitting the velocity curve into a smooth line. In the stage in braking, by extracting the middle deceleration values in Figure 7, the simulated deceleration results are compared with the theoretical results, as shown in Table 11.

In Table 11, the percentage difference of the theoretical results against the simulated results is calculated to quantify the agreement between the two results. At the III gear speed, the difference is 7.21% with the maximum design braking force, while is 2.65% with the 60% of the maximum design braking force. And at the II gear speed, the difference is 14.35% with the maximum design braking force, while is 17.58% with the 60% of the maximum design braking force. In conclusion, as for the braking deceleration, the difference between the simulated results and the theoretical results of straight-line braking is between 2.65% and 17.58%, under various braking conditions.

According to the percentage difference in Tables 10 and 11, as for the braking distance and the braking deceleration, the percentage differences between the simulation and theoretical results are calculated to be 1.22% to 17.58%, which shows the validity of the virtual model.

*3.2.3. Sensitivity Analysis of the Factors Resulting in the Deceleration Fluctuations.* In the above contact model, only the vertical stiffness and damping are considered, while the tire relaxation is regardless. Moreover, since the supporting force is an integrated response of both the stiffness and damping, from the above analysis, the independent impact of each contact characteristic on the so-called fluctuations cannot be obtained. In this case, sensitivity analysis is utilized to evaluate which factor is dominant in the causes of deceleration curves fluctuations, as shown in Figure 10(a).

In Figure 10(a), to quantify the degree of the deceleration curves fluctuations, the average difference (range) between the two neighbouring peak and valley is calculated and utilized as the measure of ordinate. Four sets of simulation experiments are carried out, separately under the change of stiffness or damping, with or without the tire relaxation. To quantify the change the contact characteristic, the relative change ratio against the original setting is calculated and utilized as the measure of abscissa. In ADAMS, the stiffness and damping can be adjusted by changing the "VERTICAL_STIFFNESS" and "VERTICAL_DAMPING" in the data subblock "[PARAMETER]"; the simulation of the tire relaxation, can be set by changing the "USE_MODE" in the data subblock "[MODEL]". The so-called "tire relaxation" means that the tire will have a lagged response because of the relaxation length in both longitudinal and lateral directions. And note that the effect of the relaxation lengths will be most obvious at low forward velocity.

As shown in Figure 10(a), in comparison with damping, the deceleration fluctuations are more sensitive to the stiffness, whether consider the tire relaxation or not. The sensitivity curve shows significant reduction as the increase of stiffness, while shows slowly decline as the increase of damping. And the higher the stiffness is, the small the sensitivity to damping is. This is reasonable because as the damper and the spring are in parallel in the contact model, if the stiffness is such high that the tire approximates to a rigid body (the deformation is zero), the damper would lose effect with no deformation. When the stiffness is 4 or 5 times (r = 4 or 5) higher than the original setting, nearly no fluctuation can be shown in the deceleration curves, as shown in Figure 10(b). Moreover, as for the same setting of stiffness and damping, the deceleration fluctuations increase slightly, no more than 0.3 $m{\cdot}s^{-2}$. The fluctuations are also not sensitive to the tire relaxation, because the initial braking velocity (under the III gear condition) is not too small to make the tire relaxation obvious.

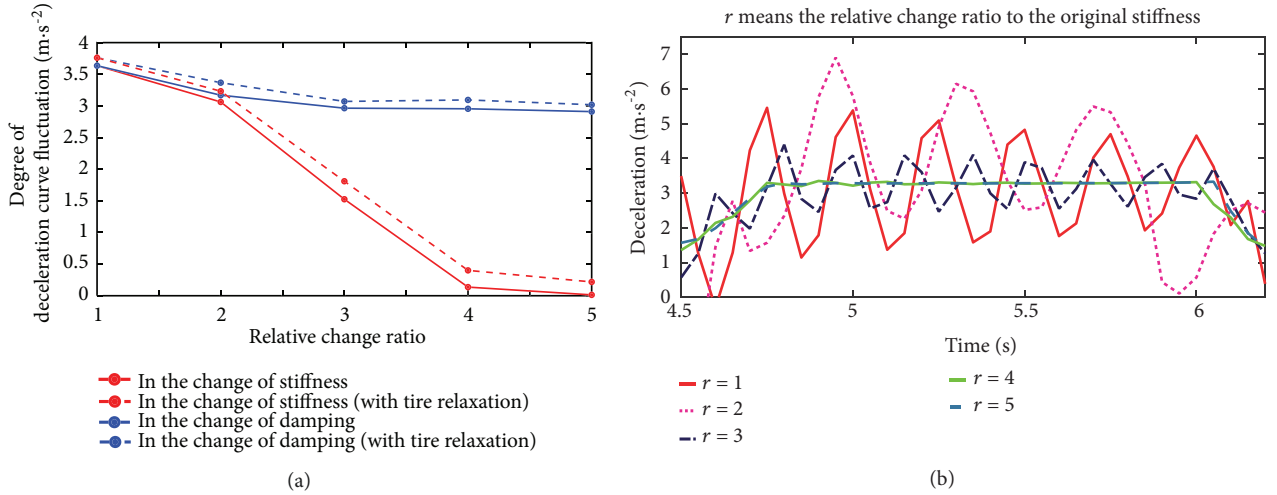


FIGURE 10: (a) Sensitivity analysis of deceleration curves fluctuations. (b) Change of the deceleration curves fluctuations with different stiffness. All the results shown in the two figures are under the braking condition of maximum design braking force, III gear condition, straight-line braking. The relative change ratio 1 means that the stiffness or damping is set to be original, as used in Figures 7–9, as shown in Table 5. The relative change ratio $r$ means that the stiffness or damping is set to be $r$ times higher than the original setting.

Hence, we can conclude that, among the three contact characteristics, stiffness is the dominant factor that results in the deceleration curves fluctuations. In contrast, damping and tire relaxation have slight influences on the fluctuations. This is to say, by adjusting the stiffness, it is easy to reduce the deceleration curves fluctuations. Figure 10(b) explicitly shows the influence of stiffness on the shape of deceleration curves.

As shown in Figure 10(b), in the stage of braking, as the increase of stiffness, the fluctuations of deceleration curves obviously reduce to a stable smooth curve (r = 4 or 5). Moreover, when the deceleration curve nearly shows no fluctuation, the stable curve approximates to the "middle value" of the wavelike curves (r = 1, 2, 3). This phenomenon further verifies the fact that the "middle value" is independent of the impact of the contact characteristics, and demonstrates the correctness of the aforementioned analyses.

### 3.3. Simulation Results and Discussion of the Braking Stability

*3.3.1. Rear Wheel Bounce.* In Figures 7(b), 7(d), 8(b), and 8(d), it can be observed that the velocity curve fluctuates significantly around 0 when the displacement curve is no longer changed. Further analysis reveals that, under the above-mentioned three kinds of braking conditions, there is obvious rear wheel bounce, which results in significant fluctuations of the mass center curve.

In order to further illustrate the reasons for the rear wheel bounce, the supporting force curve and the curve of mass center height are shown in Figure 11. Besides, the braking conditions corresponding to the bold values in Table 9 indicate the occurrence of rear wheel bounce.

In Figure 11, the supporting force acts on a single tire on the left or right side of the front and rear axles. The supporting force in Figure 11 is undulant because the UA tire model considers the stiffness and damping. The peak value of supporting force characterizes the sum of the static supporting force and the inertia force that makes the mass center rise, while the valley value of supporting force represents the difference between the static supporting force and the inertia force that makes the mass center lower. Besides, before rear wheel bounce, the ratio of the supporting force of the front wheel to that of the rear wheel is almost equal to the ratio of the distance from the mass center to the front axle (1500 mm) to that to the rear axle (1100 mm). In addition, the mean value of the supporting force acting on the front and rear axle is generally consistent with the distribution of the total weight of the combine harvester on each tire, indicating the reliability of the simulation results of the supporting force.

Further analysis of the curve of the mass center height shows that when the supporting force of the rear wheel is held constant at 0, the mass center of the combine harvester first rises and then lowers, indicating that the rear wheel bounces first and then drops under the influence of gravity. After the first time that the rear wheel comes into contact with the road again, the combine harvester experiences several bounces with damped amplitudes.

Figure 11 shows that rear wheel bounce occurs with the maximum design braking force. At this time, the mass center of the combine harvester under straight-line braking will rise to 0.8258 m and 0.5948 m with rear wheel bounce at the III and II gear speed, and will be 0.5013 m and 0.4653 m under steering braking at the III and II gear speed, respectively.

By comparing the simulation results between Figures 11(a) and 11(b), 11(c) and 11(d), it can be seen that the higher the initial braking velocity is, the higher the rear wheel bounce will be. By comparing the simulation results between Figures 11(a) and 11(c), 11(b) and 11(d), it can be observed that under the same braking conditions, the height of rear wheel bounce in steering braking is lower than that in straight-line braking. Considering the low braking efficiency

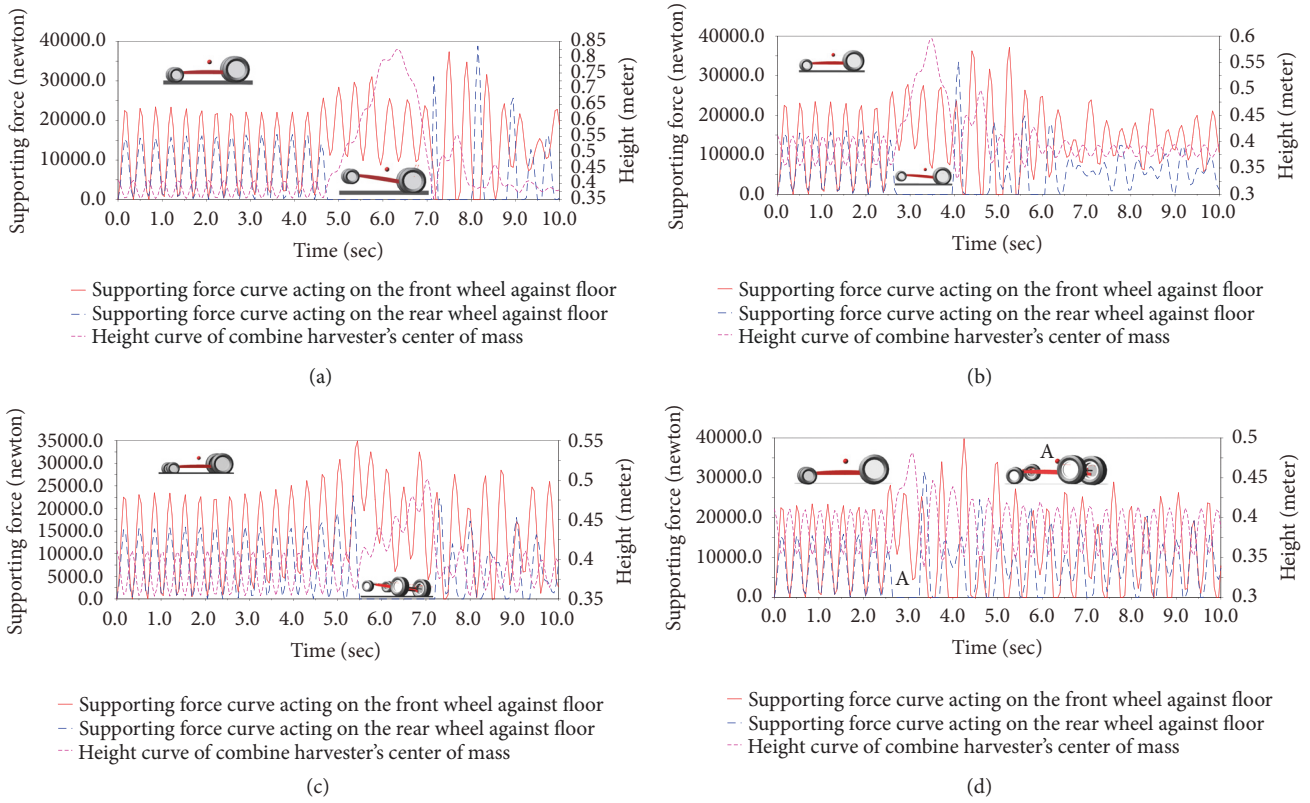


Figure 11: Analysis of the rear wheel bounce of full-load combine harvester under different braking conditions: (a) maximum design braking force, III gear condition, straight-line braking; (b) maximum design braking force, II gear condition, straight-line braking; (c) maximum design braking force, III gear condition, steering braking; and (d) maximum design braking force, II gear condition, steering braking.

of steering braking, a larger braking force should be applied to compensate for the insufficient braking performance of steering braking to ensure that the rear wheel does not bounce.

According to Figure 11 and Table 9, under the same braking conditions, 60% maximum design braking force can meet the requirements of braking performance in Table 1 and does not cause rear wheel bounce. Therefore, excessive braking force should be avoided in practice for the combine harvester. According to Table 9, for the above-mentioned braking conditions under which rear wheel bounce occurs, the braking deceleration is greater than 4.5 $m \cdot s^{-2}$, which fits the requirements in Table 1.

Moreover, as mentioned above, the theoretical calculation results show that rear wheel bounce only occurs when the braking deceleration $j \geq 16.3\ m \cdot s^{-2}$. However, in the virtual prototype simulation, rear wheel bounce occurs when the braking deceleration is greater than 5.5234 $m \cdot s^{-2}$. Compared with the theoretical results, the simulation results are closer to the threshold value of 4.5 $m \cdot s^{-2}$ in Table 1. This is to say, in comparison with the theoretical results, the peak deceleration extracted from the simulated results, is closer to the real experimental results (i.e., the field-test results) in the condition of the rear wheel bounce. Hence, the simulated peak deceleration can provide a more valuable reference for predicating and preventing the phenomenon of the rear wheel bounce. This is because the virtual prototype simulation takes complex and multiple contact characteristics into consideration, which accounts for the differences between the theoretical results and simulation results. As the rear wheel bounce is not only related to the capsizing moment, but also associated with the contact characteristics (e.g., the stiffness and damping between the tire and the road), the virtual prototype simulation provides a more comprehensive and reasonable results about the rear wheel bounce, than the theoretical results.

*3.3.2. Braking Directional Stability.* The braking directional stability is related to the uneven braking force, the adhesion coefficient and the initial velocity.

In order to simulate the uneven left and right braking force, in the simulation experiments, the uneven coefficients of braking force between the left and right brake were set as 0~0.3 with a step size of 0.05 (see Figure 12). At a certain steering angle and under the condition of rear wheel locking, the influence of uneven braking force on braking directional stability of full-load combine harvester was simulated and analyzed (see Figure 12).

Figure 12 shows that when the rear wheel is locked, whether it be straight-line braking or steering braking, the lateral displacement of the combine harvester is significantly larger than that when the rear wheel is free. In addition, as

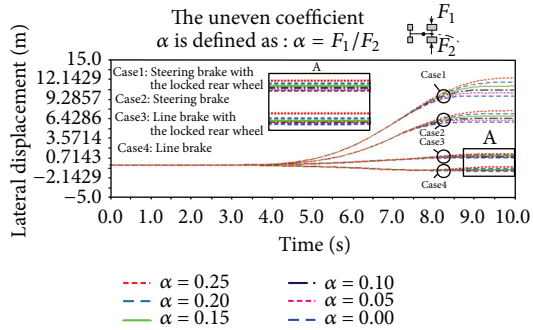


Figure 12: Influence of uneven braking force on lateral displacement.

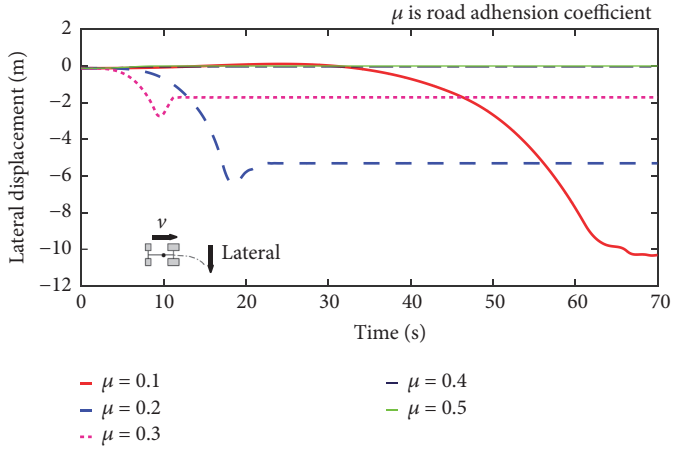


Figure 13: Influence of road adhesion coefficients on lateral displacement.

the uneven coefficient of braking force increases, the lateral displacement rises accordingly.

Further analysis shows that when the uneven coefficient changes to the same extent (such as 0.05~0.10 and 0.15~0.20), there are greater increases in lateral displacement when the rear wheel is locked than when the rear wheel is unlocked. That is to say, when the rear wheel is locked, the lateral displacement is more sensitive to the uneven coefficient. In addition, according to Figure 12, with the same value of time, the absolute difference of lateral displacement between the two different curves whose value of uneven coefficient $\alpha$ are the same in Case 1 and Case 2 is obviously greater than that in Case 3 and Case 4, indicating that the lateral slip caused by rear wheel locking in steering braking is more serious than that in straight-line braking.

It should be noted that in the case of straight-line braking, whether the rear wheel is locked or unlocked, the combine harvester will exhibit a tendency to slip in the opposite direction, and the cause is analyzed as follows. There are two main forces that cause the combine harvester to slip: one is the mass imbalance force due to the left deviation of part arrangement in the steering axle (Figure 4(b)), which will result in a leftward sideslip force $F_{lm}$; another is the sideslip force $F_{rb}$ toward right caused by the uneven braking force, which is essentially a kind of friction. When the rear wheel is locked, the $F_{rb}$ will be significantly reduced to be lower than $F_{lm}$, resulting in the sliding of the combine harvester to the left side. When the rear wheel is unlocked, $F_{rb}$ is greater than $F_{lm}$, leading to the sliding of the combine harvester to the right side.

*3.3.3. Influence of Adhesion Coefficient and Initial Velocity on Braking Directional Stability.* In order to simulate the different adhesion coefficients, in the simulation experiments, the adhesion coefficients were set as 0.1~0.9 with a step size of 0.2 (see Figure 13). Figure 13 shows the lateral displacement simulation curve of full-load combine harvester at straight-line braking with different road adhesion coefficients, under the braking conditions of III gear speed and 60% of maximum design braking force.

Figure 13 reveals that, for the road with an adhesion coefficient above 0.7, the lateral slippage of the combined harvester in braking is almost 0; for the road with an adhesion coefficient of 0.1 to 0.5, the lateral slippage of the combine harvester in braking significantly increases with decreasing road adhesion coefficients. The simulation results show that, under the same braking conditions, the lower the road adhesion coefficient is, the greater the lateral slippage of combine harvester in braking will be.

According to Figure 13, for the road surface with an adhesion coefficient above 0.7, lateral slippage almost does not occur. In addition, the common adhesion coefficient

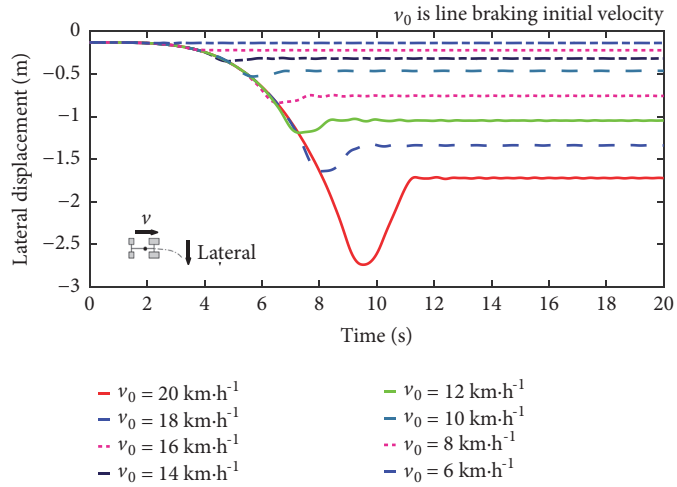


Figure 14: Influence of different initial velocities of straight-line braking on lateral displacement.

for combine harvester working is about 0.5 [9]. Therefore, the adhesion coefficient was set as 0.5 for investigating the influence of initial braking velocity on lateral slippage.

In order to simulate the different braking velocities, in the simulation experiments, the braking velocities were set as 6~20 km·h$^{-1}$ with a step size of 2 km·h$^{-1}$ (see Figure 14). Figure 14 shows the lateral displacement simulation curve of full-load combine harvester at straight-line braking with different initial braking velocities.

In Figure 14, the lateral slippage is on a rapid rise when the initial braking velocity changes from 10 km·h$^{-1}$ to 20 km·h$^{-1}$; however, when the initial braking velocity is lower than 10 km·h$^{-1}$, the lateral slippage is almost 0. The simulation results show that, under the same braking conditions, the higher the initial braking velocity is, the more significant the lateral slippage will be. According to Figures 13 and 14, the working speed should be stabilized at a low level to prevent significant lateral slippage, especially on slippery road with a low adhesion coefficient.

Furthermore, in both Figures 13 and 14, the lateral slippage shows increases first, followed by decreases with the road adhesion coefficient of 0.5. This phenomenon indicates that the locking of the front wheel occurs before that of the rear wheel, which has a correction effect on the lateral slippage [8]. In this case, the synchronous adhesion coefficient of the combine harvester in virtual prototype should not be lower than 0.5, which is consistent with the theoretically calculated value of 0.76 in Figure 3.

## 4. Conclusions

In this study, extensive theoretical and simulation results have demonstrated that, other than traditional field-test method, our proposed novel method can provide an effective way for designing and evaluating the chassis braking system of combine harvesters

From the simulation results, the following conclusions can be drawn:

(1) The braking efficiency is higher with greater braking force or lower initial braking velocity, whether it be straight-line braking or steering braking. Compared with straight-line braking, steering braking has lower efficiency.

(2) In terms of braking stability, the lateral slippage increases significantly with lower road adhesion coefficients, higher initial braking velocities, or the locking of the rear wheel, resulting in a dramatic decline of the braking directional stability. In addition, under the same braking conditions, rear wheel bounce is less likely to occur under steering braking or full-load conditions.

(3) The simulated results are in agreement with the theoretical results, as the minimum percentage difference is 1.22% and 2.65% for the braking distance and deceleration respectively. Moreover, the simulated results can provide more comprehensive and reasonable prediction of the rear wheel bounce and are closer to the real experimental results (i.e., the field-test results), than the theoretical results. In short, the virtual prototype simulation is validated to be valuable and effective for evaluating the braking efficiency and the braking directional stability of the combine harvester and providing the basis for designing the combine harvester. In addition, with the road adhesion coefficient of 0.5, the lateral slippage in simulation first increases and then decreases, indicating that the synchronous adhesion coefficient is greater than 0.5, which meets the theoretical value of 0.76 under the full-load condition. Above all, the simulation results are in agreement with the theoretical results, proving the validity of the virtual prototype.

## Data Availability

The data used to support the findings of this study are included within the article.

## Conflicts of Interest

The authors declare that there are no conflicts of interest regarding the publication of this paper.

## Acknowledgments

This work was supported by National Natural Science Foundation of China [Grants nos. 51875230 and 51405178].

## References

[1] Y. S. Kim, S. D. Lee, Y. J. Kim et al., "Effect of tractor travelling speed on a tire slip," *Korean Journal of Agricultural Science*, vol. 45, no. 1, pp. 120–127, 2018.

[2] B. Xie, J. Li, Q. Lu et al., "Simulation and experiment of virtual prototype braking system of combine harvester," *Transations of the Chinese Society of Agricultural Engineering*, vol. 30, no. 4, pp. 18–24, 2014 (Chinese).

[3] C. Li, X. Li, Z. Wang et al., "Effect of load transfer of tractor-semitrailer on cornering braking stability," *Journal of Traffic and Transportation Engineering*, vol. 14, no. 2, pp. 68–74, 2014.

[4] C. Li, "Effect of road adhesion coefficient on tractor-semitrailer cornering braking stability," in *Proceedings of the International Conference on Mechanical Engineering and Control Systems*, pp. 166–170, World Scientific, Wuhan, China, January 2015.

[5] P. Gurevicius and A. Janulevicius, "Tractor MFWD braking deceleration research between different wheel drive," in *Proceedings of the 16th International Scientific Conference Engineering for Rural Development*, vol. 6, p. 854–859, Latvia University of Agriculture Faculty of Engineering, Jelgava, Latvia, 2017.

[6] C. Zong, T. Zhu, C. Wang et al., "Multi-objective stability control algorithm of heavy tractor semi-trailer based on differential braking," *Chinese Journal of Mechanical Engineering*, vol. 25, no. 1, pp. 88–97, 2012.

[7] M. Nastasoiu and N. Ispas, "Comparative analysis into the tractor-trailer braking dynamics: Tractor with single axle brakes, tractor with all wheel brakes," *Central European Journal of Engineering*, vol. 4, no. 2, pp. 142–147, 2014.

[8] T. D. Gillespie, *Fundamentals of Vehicle Dynamics*, Society of Automotive Engineers, Inc, Pennsylvania, Pa, USA, 1992.

[9] S. Sun, X. Li, D. Yue et al., "Study on the load distribution influenced on the braking performance of derivate tractor," *Journal of Agricultural Mechanization Research*, vol. 3, pp. 247–249, 2004 (Chinese).

[10] GB 16151.12-2008, "Technical requirements of operating safety for agricultural machinery—Part 12," Grain combine-harvester.

[11] GB/T 14248-2008, "Determination of braking performance for harvesting machinery".

[12] G. Gim and P. E. Nikravesh, A three dimensional tire model for steady-state simulations of vehicles, SAE Paper 1993-931913, 1993.

[13] J. A. Lines and K. Murphy, "The stiffness of agricultural tractor tyres," *Journal of Terramechanics*, vol. 28, no. 1, pp. 49–64, 1991.

[14] C. R. Carlson and J. C. Gerdes, "Consistent nonlinear estimation of longitudinal tire stiffness and effective radius," *IEEE Transactions on Control Systems Technology*, vol. 13, no. 6, pp. 1010–1020, 2005.

[15] R. Wang and J. Wang, "Tire-road friction coefficient and tire cornering stiffness estimation based on longitudinal tire force difference generation," *Control Engineering Practice*, vol. 21, no. 1, pp. 65–75, 2013.

[16] G. Baffet, A. Charara, and D. Lechner, "Estimation of vehicle sideslip, tire force and wheel cornering stiffness," *Control Engineering Practice*, vol. 17, no. 11, pp. 1255–1264, 2009.

[17] L. Gu, Y. Zhou, Y. Chen et al., "Simulation research on spatial vibration response of tractor based on ADAMS," *Journal Machine Design*, vol. 31, no. 01, pp. 80–84, 2014 (Chinese).

[18] J. Han, Y. Wang, and K. Zhou, "Research on an estimate method of longitudinal tire stiffness based on patten search," *Transactions of the Chinese Society for Agricultural Machinery*, vol. 38, no. 12, pp. 28–31, 2007 (Chinese).

[19] X. Ning, B. Meng, and W. Lei, "Virtual prototype solid modeling and application of heavy truck brake," *Journal of System Simulation*, vol. 18, no. 8, pp. 2187–2189, 2006.

[20] B. Ozdalyan and M. V. Blundell, "Anti-lock braking system simulation and modelling in ADAMS," in *Proceedings of the International Conference on Simulation '98*, pp. 140–144, IET, London, UK, September–2 October 1998.

[21] X. Zhang, B. Yang, C. Yang et al., "Research on ABS of multi-axle truck based on ADAMS/Car and Matlab/Simulink," *Procedia Engineering*, vol. 37, no. 2, pp. 120–124, 2012.

[22] D. Wan, *Structural optimization design of drum brake based on ADMAS [M.S. Thesis]*, Hebei University of Technology, Tianjin, China, 2011.

[23] I. Nurzaki, A. S. Abdullah, and R. Ramli, "Experimental validation of vehicle dynamic characteristics of a virtual heavy vehicle model," *Journal of Mechanical Engineering*, vol. 4, no. 5, pp. 131–143, 2017.

[24] J. Yan, L. Wang, D. Zhang et al., "Investigation of friction force between car tire and road," *Journal of Shandong University of Technology*, vol. 21, no. 6, pp. 5–10, 2007 (Chinese).

[25] E. Velenis, P. Tsiotras, C. Canudas-De-Wit, and M. Sorine, "Dynamic tyre friction models for combined longitudinal and lateral vehicle motion," *Vehicle System Dynamics*, vol. 43, no. 1, pp. 3–29, 2005.